

Electronic structure of BaSnO₃ investigated by high-energy-resolution electron energy-loss spectroscopy and *ab initio* calculations

Authors: Hwanhui Yun, Mehmet Topsakal, Abhinav Prakash, Koustav Ganguly, Chris Leighton, Bharat Jalan, Renata M. Wentzcovitch, K. Andre Mkhoyan*, and Jong Seok Jeong*

Department of Chemical Engineering and Materials Science, University of Minnesota, Minneapolis, Minnesota 55455, USA

*Corresponding Authors: mkhoyan@umn.edu (K.A.M), jsjeong@umn.edu (J.S.J)

ABSTRACT

There has been growing interest in perovskite BaSnO₃ due to its desirable properties for oxide electronic devices including high electron mobility at room temperature and optical transparency. As these electronic and optical properties originate largely from the electronic structure of the material, here the basic electronic structure of epitaxially-grown BaSnO₃ films is studied using high-energy-resolution electron energy-loss spectroscopy in a transmission electron microscope and *ab initio* calculations. This study provides a detailed description of the dielectric function of BaSnO₃, including the energies of bulk plasmon excitations and critical interband electronic transitions, the band structure and partial densities of states, the measured band gap, and more. To make the study representative of a variety of deposition methods, results from BaSnO₃ films grown by both hybrid molecular beam epitaxy and high pressure oxygen sputter deposition are reported.

I. INTRODUCTION

Perovskite structure BaSnO_3 has gained increasing attention recently as a candidate material for next-generation oxide electronic devices. This material has shown notably high electron mobility at room temperature, reported to be up to $320 \text{ cm}^2\text{V}^{-1}\text{s}^{-1}$ in bulk single crystal [1,2] and up to $150 \text{ cm}^2\text{V}^{-1}\text{s}^{-1}$ in epitaxial thin films of La-doped BaSnO_3 [3], with good optical transparency in the visible region. These properties are desirable in transparent conducting materials for solar cells, displays, high-mobility channels for transistors, and other applications [4-8]. Recent successes in thin film growth of epitaxial BaSnO_3 using vacuum deposition techniques [3,9-11] have opened up new possibilities to engineer various heterostructures based on this material, and to improve its electron mobility through defect control, polarization doping, etc. [6,8,12,13]. However, to optimize the potential utility of this material, it is essential to understand the electronic structure of BaSnO_3 in order to elucidate the mechanisms for high mobility. To this end, there have been several previous *ab initio* studies and optical measurements to understand various properties of BaSnO_3 . Electronic band structures have been calculated [14-17], and the conduction band edge effective mass [18], band gap energy [8,19,20], and dielectric constant [21] have been experimentally determined.

Here, we report comprehensive information on the electronic structure of BaSnO_3 using high-energy-resolution electron energy-loss spectroscopy (EELS) in a scanning transmission electron microscope (STEM). We have acquired high-energy-resolution EELS spectra at elemental edges and compared them with *ab initio* predictions to examine the electronic structure of BaSnO_3 . The low-loss region (0-50 eV) of EELS has been used to study dielectric properties, including interband electronic transitions and plasmon excitations. In the high-loss region (>50 eV), fine structure of core-edges reveals the details of the conduction band by directly probing the element-specific empty density of states (DOS) of the material. Good agreement between experimentally measured EELS spectra and the results of *ab*

initio calculations provides critical reliability for the details of the electronic structure of BaSnO₃ reported here.

II. METHODS

A. Sample preparation

Two epitaxial, single-phase BaSnO₃ films were grown on SrTiO₃(001) and LaAlO₃(001) substrates by hybrid molecular beam epitaxy (MBE) [9] and high pressure oxygen sputter deposition [22], respectively. A nominal thickness was 72 and 28 nm for the BaSnO₃ films on SrTiO₃ and LaAlO₃, respectively. The as-grown BaSnO₃ film on LaAlO₃ was further annealed in ultra-high vacuum ($<10^7$ Torr) at 900 °C for 4 h. This process dopes the BaSnO₃ film with oxygen vacancy to $\sim 5 \times 10^{19} \text{cm}^{-3}$ [22]. Cross-sectional transmission electron microscopy samples were prepared by using a focused ion beam (FEI Quanta 200 3D) lift out method, where the samples were thinned by a 30 kV Ga-ion beam and then cleaned with a 5 kV Ga-ion beam. The samples were further polished by Ar-ion milling using a Fischione 1010 ion mill and a Gatan precision ion polishing system. This process of sample preparation provides relatively damage-free, electron-transparent samples with thickness in the range 20-60 nm. The relative sample thickness (t) was estimated to be $t/\lambda_p = 0.25-0.50$ [23] using the EELS log-ratio method (λ_p is mean-free-path of plasmon excitations) [24].

B. STEM imaging and EELS data acquisition

STEM imaging and EELS measurements were carried out using an aberration-corrected FEI Titan G2 60-300 (S)TEM equipped with a CEOS DCOR probe corrector, a Schottky extreme field emission gun

(X-FEG), a monochromator, and a Gatan Enfinium ER spectrometer. The microscope was operated at 200 keV. The semi-convergence angle of the STEM probe was 15 mrad and the beam current was set to 50 pA. High-angle annular dark-field (HAADF) images were recorded with a detector angle of 42-200 mrad; the collection angle of the EELS was 29 mrad. A dual EELS mode, which simultaneously collects the low-loss region including a zero-loss peak (ZLP) and high-loss region, was used to correct the energy alignment, when needed. Energy dispersions of 0.05 and 0.1 eV per channel were used to measure low-loss and core-loss data of both BaSnO₃ films, while EELS data for detailed analysis of interband electronic transitions were acquired with an energy dispersion of 0.01 eV per channel. Energy resolutions for these dispersion values, estimated from the full-width at half maximum (FWHM) of the ZLPs, were 0.4, 0.25, and 0.13 eV for 0.1, 0.05, and 0.01 eV per channel, respectively. For an accurate determination of peak positions, the alignment and dispersion values of the spectrometer were calibrated using reference peaks of Si $L_{2,3}$ of SiO₂ (108.3 eV), π^* of graphite (285.37 eV), and Ni L_3 of NiO (852.75 eV) [24]. Several EELS spectra from equivalent regions were acquired and summed to reduce the effects from very small, but unavoidable specimen damage by the STEM electron beam and to increase the signal-to-noise ratio. All EELS spectra were obtained from the central regions of BaSnO₃ films in order to minimize the influence of the film-substrate interface and surface.

C. *Ab initio* calculations

Ab initio calculations were performed using the WIEN2K code [25-27]. A generalized gradient approximation (GGA) using Perdew-Burke-Ernzenhof (PBE) parametrization [28] was adopted for the electronic exchange and correlation functional. The Brillouin zone was sampled at a 16×16×16 shifted k -point grid using the tetrahedron method [29]. The wave functions were expanded in spherical harmonics

inside non-overlapping atomic spheres of radius R_{MT} (muffin-tin radii) and in plane waves for the remaining space of the unit cell. R_{MT} values for Ba, Sn, and O were set at WIEN2K defaults. The plane wave expansion in the interstitial region was determined by a cut-off wave vector chosen to be $k_{\text{max}} = 7.0/R_{\text{MT}}$. Empty states up to 4.0 Ry (= 54.4 eV) above the Fermi level, E_{F} , were included in the calculations. Frequency dependent dielectric matrix calculations within the independent particle random phase approximation were performed using the OPTIC module of WIEN2K, as detailed in Ref. [30]. O K edge EELS simulations were performed using the TELNES3 module of WIEN2K with calculation parameters from the experimental setup. Core-hole effects were included. Because calculations using GGA are known to result in a smaller band gap than experimental results [15,17], the band gap was adjusted to the measured value.

III. RESULTS AND DISCUSSION

Figure 1 shows HAADF-STEM images of the BaSnO₃ films that were used for EELS analysis in this work. From the HAADF-STEM images, the film thickness was measured to be 72 and 30 nm for the BaSnO₃ films on SrTiO₃ and LaAlO₃, respectively. High-resolution HAADF-STEM images demonstrate that these BaSnO₃ films are indeed epitaxially grown on the substrates, and form a sharp interface with relatively low surface roughness.

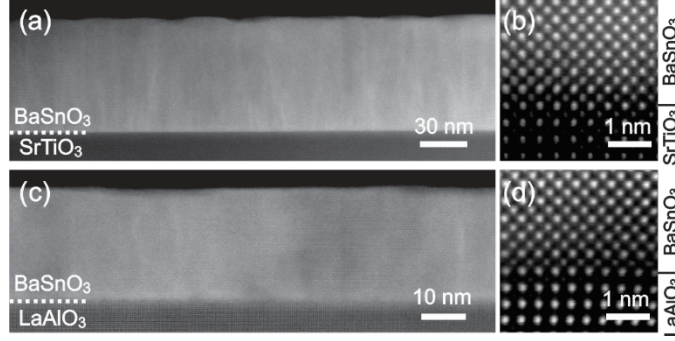


FIG. 1. Low-magnification and high-resolution HAADF-STEM images of BaSnO₃ films: (a,b) 72 nm-thick BaSnO₃ film grown on a SrTiO₃(001) substrate by hybrid MBE and (c,d) 30 nm-thick BaSnO₃ film grown on a LaAlO₃(001) substrate by high pressure oxygen sputter deposition. Atomic-resolution HAADF-STEM images of each film at the interfaces are shown in (b) and (d). The images were filtered using a standard Wiener filter, where a Butterworth filter was applied to remove high-frequency noise and amorphous components of the images [31,32]. The parameters used for the filter were: 5 for the step size of the iteration; 5 % for delta % (the upper limit of the % of pixels to be changed by each iteration); 20 for the number of cycles; 2 for the order of the Butterworth filter; and 0.5 for the FWHM of the Butterworth filter.

A. Calculated dielectric function and band structure

The calculated dielectric function of BaSnO₃ is shown in Fig. 2. The complex dielectric function $\epsilon(E) = \epsilon_1(E) + i\epsilon_2(E)$ describes how the electron gas in materials responds to an applied electromagnetic field [24,33-38]. The energy where the real part of the dielectric function, $\epsilon_1(E)$, changes from negative to positive, evidences a bulk plasmon due to collective oscillations of the electrons. The calculated $\epsilon_1(E)$ indicates that in BaSnO₃ bulk plasmons are generated at 15.2 and 26.6 eV, marked as I and E_P in Fig. 2, respectively. In the imaginary part of the dielectric function, $\epsilon_2(E)$, peaks correspond to the direct interband electronic transitions [24,33-38]. Distinguishable peaks in $\epsilon_2(E)$ are marked with arrows and labeled in Fig. 2, and details are discussed in later sections.

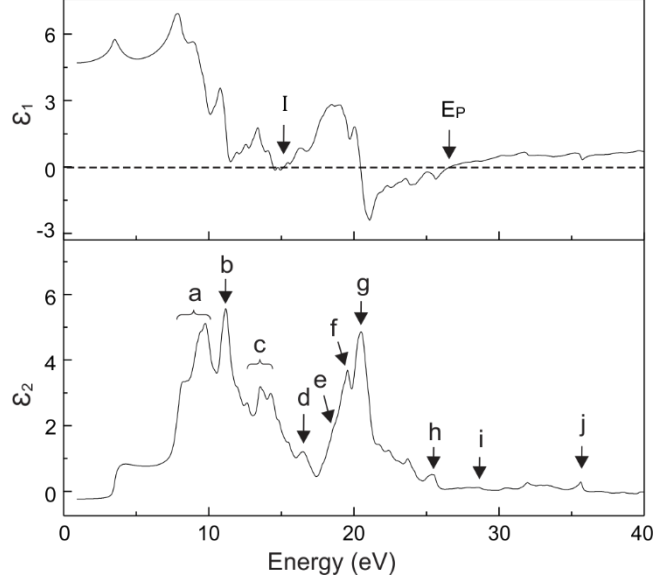


FIG. 2. The calculated real, ϵ_1 , and imaginary, ϵ_2 , parts of the dielectric function of BaSnO_3 . The bulk plasmon energies (I , E_p) in ϵ_1 and direct interband transition peaks (a to j) in ϵ_2 are marked.

The calculated band structure and DOS of BaSnO_3 are shown in Fig. 3. The results are essentially consistent with previous reports [16,17,19,39,40]. The conduction band minimum is positioned at the Γ point (0, 0, 0) and the valence band maximum is at the M point (0.5, 0.5, 0) in reciprocal space. Figure 3(b) shows that the lower conduction bands from 3 to 8 eV consist predominantly of s and p states of Sn and O, and the conduction bands above 8 eV are mainly composed of d and f states of Ba. The O $2p$ states are dominant in the upper valence band, and high-density Ba $5p$ states are found at around -10 eV.

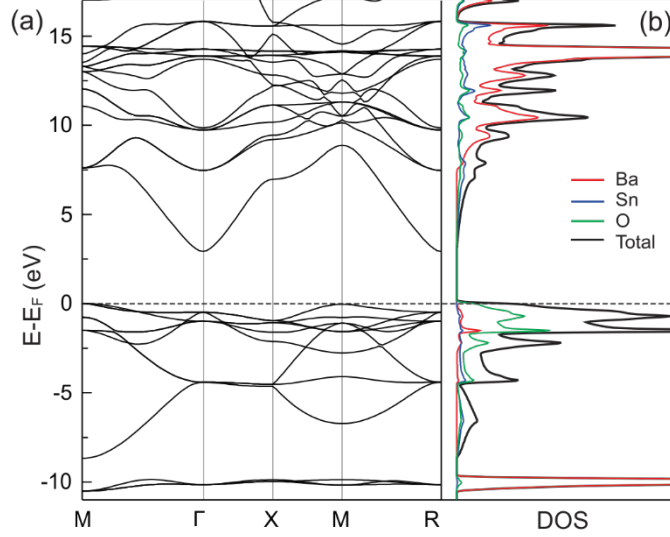


FIG. 3. Calculated band structure (a) and elementally resolved and total DOS (b) of BaSnO₃. Here E_F is at the valence band maximum.

B. Band gap measurement

The band gap of BaSnO₃ films was measured using high-energy-resolution low-loss EELS data. To measure the band gap from the low-loss EELS data, the ZLP was removed as follows: (1) a zero-loss EELS spectrum was acquired in vacuum, (2) it was scaled to fit with the low-loss EELS spectra in the 1 to 2.5 eV range using a multiple linear regression method, and (3) the fitted zero-loss EELS spectrum was subtracted from the low-loss EELS data. To improve statistics, 22 spectra from the BaSnO₃ film on SrTiO₃ and 14 spectra from the BaSnO₃ film on LaAlO₃ were acquired and analyzed. One representative example is shown in Fig. 4. The onset value of the ZLP-subtracted spectrum indicates the band gap energy. The measured band gap energy for BaSnO₃ films on SrTiO₃ and LaAlO₃ substrates was 3.0 ± 0.1 eV and 3.1 ± 0.2 eV, respectively. To confirm the validity of this method, the same analysis was applied to the SrTiO₃ substrate and the resulting band gap energy was 3.3 ± 0.1 eV, which is consistent with well documented SrTiO₃ band gap energy of 3.25 eV [41]. The band gap energy of BaSnO₃ films from our measurements

are compared with the values reported in the literature in Table I. A band gap energy of 3.0 eV is used for all subsequent analyses.

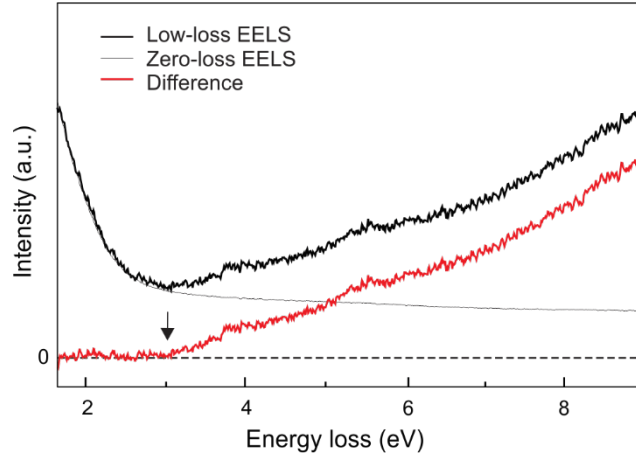


FIG. 4. A high-energy-resolution low-loss EELS spectrum obtained from a BaSnO₃ film on a LaAlO₃ substrate. The zero-loss EELS, obtained in vacuum, was fitted to the low-loss EELS spectrum and then subtracted from the spectrum to get the difference. The onset of the difference, which corresponds to the band gap, is indicated by an arrow.

TABLE I. Experimentally-measured band gap energy (E_g) of BaSnO₃ from the literature.

E_g (eV)		Method	Ref.
Direct	Indirect		
	3.0 ± 0.1	Low-loss EELS	this work
	3.1 ± 0.2		
3.56 ± 0.05	2.93 ± 0.05	Ellipsometry	[8]
3.12	2.85	Diffuse reflectance	[42]
3.1	2.95	Transmittance	[43]
3.4		Reflectance	[38]

C. Low-loss EELS analysis

Low-loss EELS spectra were measured on the BaSnO₃ films and compared with the electron energy-loss function calculated from the dielectric function. The energy-loss spectrum of incident probe electrons, which travel through a sample and act as an electromagnetic wave, can be deduced from the

imaginary part of the inverse dielectric function, as it is proportional to $Im[-1/\epsilon]$ (or $\epsilon_2/(\epsilon_1^2 + \epsilon_2^2)$) [24,33-38]. To account for the energy spread of the incident electron beam, the calculated $Im[-1/\epsilon]$ was convolved with a Gaussian function [44]. The FWHM of the Gaussian function was set to be the FWHM of the ZLP for each data set. The measured low-loss EELS spectra from BaSnO₃ films and the calculated $Im[-1/\epsilon]$ are then compared, as can be seen in Fig. 5. For more quantitative analysis, the peak positions are compared in Table II. The overall shape and peak positions from the calculation and the experimental measurements are in good agreement. However, there are noticeable differences between the calculated $Im[-1/\epsilon]$ and the measured low-loss EELS spectra because: (1) the calculation underestimates damping of plasmon oscillations [24,33] and (2) contributions from surface plasmons, Cerenkov radiation [45,46], and core-loss Sn $N_{4,5}$ edge are not included in the calculation.

In low-loss EELS, a bulk plasmon peak is observed at 26.1 eV (denoted as E_P in Fig. 5), whereas it appears at 26.6 eV in the calculated $Im[-1/\epsilon]$ (see Fig. 2). This discrepancy is due to plasmon damping. Plasmon damping induces broadening and shift of plasmon peaks; the plasmon linewidth, ΔE_P , which is the FWHM of a plasmon peak, is determined by the plasmon damping constant, and the plasmon peak position shifts from E_P to a lower value of $\sqrt{E_P^2 - (\Delta E_P^2/2)}$ [24]. The plasmon damping constant is governed by how fast plasmons decay by transferring their energy to an alternative mechanism, in the majority of cases to interband electronic excitations [24]. In a film, the energy transfer to the interband electronic excitations is facilitated by the extra energy or momentum from the lattice or phonons, which is followed by the faster plasmon damping. In addition, plasmons also decay via defects present in the films and through direct generation of phonons [47,48]. Because phonons and defects are not considered in the calculations, the experimental plasmon peak appears at the lower energy of 26.1 eV compared to the calculated value of 26.6 eV [49]. An additional plasmon peak at 15.2 eV is also predicted from the calculated dielectric function, as discussed above. We speculate that this plasmon represents oscillations

of electrons in a subsidiary band near the valence band, but this needs further study. Due to several peaks from interband transitions and surface plasmons, this plasmon peak is not clearly identifiable in the low-loss EELS data. As stated above, the experimental low-loss EELS includes other contributions, such as surface plasmon peaks and the Sn $N_{4,5}$ edge, in contrast to the calculation. The surface plasmon peak is expected to be at around 18.8 eV from $E_{SP} = E_p / \sqrt{2}$ [24,33,34,38]; however, such a peak is not discernible as it is superimposed on strong interband transition peaks. The Sn $N_{4,5}$ edge should also be present starting from around 24 eV [50], but is not readily apparent due to overlap with the bulk plasmon and interband transition peaks.

The peaks, labeled from a to k in low-loss EELS in Fig. 5(a), result from interband electronic transitions (see Fig. 2). More detailed fine structure of these peaks is shown in Fig. 5(c), where the peaks from a to e are further resolved and labeled using subscripts. The second bulk and surface plasmon peaks (I and II), which were discussed above, are also presented. To interpret the interband transition peaks, the energy levels with high-density electronic states were examined from a calculated partial density-of-states (pDOS), and the possible interband electronic transitions from valence band to conduction band were investigated within the selection rules [51]. For easy comparison, the peaks predicted from the possible interband transitions are indicated as labeled from a to g in Fig. 5(c). The energies of the majority of these interband electronic transition are identified from experimental low-loss EELS spectra as well as from calculated imaginary part of the dielectric function and from peaks of $Im[-1/\epsilon]$. The results are tabulated, and the assigned interband electronic transitions are summarized, in Table II.

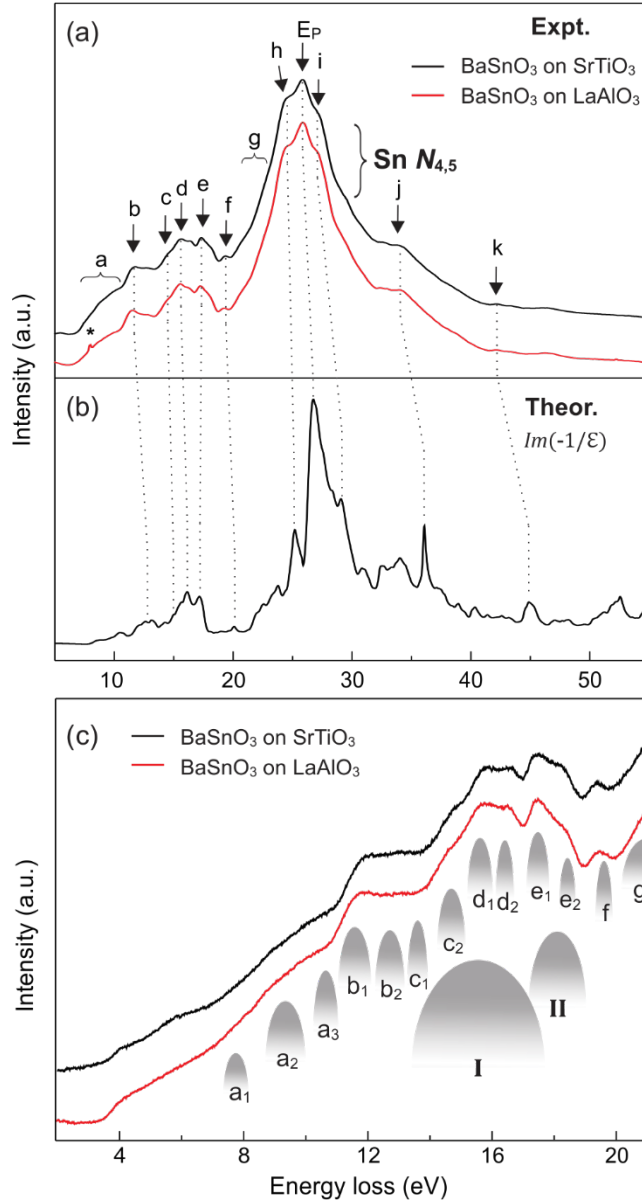


FIG. 5. Comparison of experimental low-loss EELS spectra from the two BaSnO₃ films (a), and calculated $Im[-1/\epsilon]$ (b). The peaks from interband electronic transitions are labeled from a to k. The bulk plasmon peak, E_P , and the Sn $N_{4,5}$ edge are also indicated. The artifact peak from the ZLP is marked by an asterisk. (c) High-energy-resolution low-loss EELS spectra from the same BaSnO₃ films. Possible interband transitions, predicted from theory, are indicated with the labels. The peaks I and II represent predicted second bulk and surface plasmon peak, respectively.

TABLE II. Peak positions (in eV) from plasmon excitations and interband electronic transitions. The peaks are labeled as in Figs. 2 and 5 and compared to the predicted transitions from the calculated ϵ , $Im[-1/\epsilon]$, and pDOS with assignments.

Group	Peaks	Experiment	Theory			Assignment	
Plasmon	E_p	26.1	26.6			1 st Bulk plasmon	
	I	-	15.2			2 nd Bulk plasmon	
	II	-	18.8			Surface plasmon	
			from ϵ_2	from $Im[-1/\epsilon]$	from pDOS	Initial state	Final state
Interband	a_1	-	8.3	8.4	7.8, 8.5	O 2p	Sn 6s
	a_2	-	9.5, 9.8	9.6	9.3, 10.1	O 2p	Sn 6s
	a_3	-	10.4	10.3	10.2, 10.9	O 2p	Ba 5d
	b_1	~12	11.2, 12.0	11.9, 12.4	11.4, 12.1,	O 2p	Sn 6s
					12.7		
					11.2, 11.7,	O 2p	Ba 5d
					12.0		
	b_2	~13	12.7	12.9	11.4, 12.1	Sn 4p	Sn 6s
					12.7	O 2p	Sn 6s
					12.8	O 2p	Ba 5d
	c_1	~14	13.6	13.7, 14.0	13.7	O 2p	Ba 5d
					13.6	Sn 4d, Ba 4d	Ba 4f
					13.7	Sn 4p	Ba 5d
	c_2	~15	14.4, 14.8	~15	14.7	O 2p	Sn 6s
					14.8	O 2p	Ba 5d
					14.4	Sn 4d, Ba 4d	Ba 4f
					14.8	Sn 4p	Ba 5d
	d_1	15.8	15.5	15.9	15.6	Sn 4d, Ba 4d	Ba 4f
	d_2	16.6	16.5	-	16.4	Sn 4d, Ba 4d	Ba 4f
	e_1	17.5	17.1	17.0	17.1, 17.8	Sn 4d, Ba 4d	Ba 4f
17.2					Ba 5p	Sn 6s	
e_2	18.2	18.5	-	18.5	Sn 5s	Sn 5p	
f	19.4	19.6	19.9	19.5	O 2p	Sn 5d	
				19.4	Sn 5s	Sn 5p	
				19.5	Ba 5p	Ba 5d	
				20.5	Ba 5p	Sn 6s	
g	~21	20.5	-	20.3	O 2p	Sn 5d	
				20.6	Ba 5p	Ba 5d	
				20.5	Ba 5p	Sn 6s	
h	24.7	25.4	24.9	-	-	-	
i	27.3	28.6	28.8	-	-	-	
j	34.3	35.7	35.8	-	-	-	
k	42.4	44.5	44.6	-	-	-	

D. Core-loss EELS analysis

High-energy-resolution O K edge EELS spectra were measured from BaSnO₃ films and compared with the O K edge simulation result generated using the WIEN2K code, where a double differential cross

section for core-level electronic transitions is calculated from the already calculated DOS; $\frac{\partial^2 \sigma}{\partial E \partial \Omega} \propto \sum_{i,f} |M_{i,f}|^2 \text{DOS}(E)$, where Ω is the scattering solid angle and $M_{i,f}$ is the transition matrix element [52,53]. This double differential cross section is then integrated using experimental STEM probe convergence and EELS collection angles [25,54]. An energy spreading of the incident electron beam was implemented by convolving the simulation result with a Gaussian function with the FWHM of the ZLP. Next, the natural energy broadening, which arises from the lifetime of the electrons in the initial and final states of excitation, was taken into account [24,55,56]. The energy level width of the initial O 1s state, Γ_i , is as small as 0.153 eV. In contrast, the energy level width of the final state, Γ_f , is considerable and varies with energy relative to the conduction band minimum (or onset energy of core-loss edge). The Γ_f for O 2p increases from 0 to 6 eV with increasing the energy from 0 to 40 eV above the onset energy [55]. The energy broadening due to the lifetime effect (for both initial and final states) can be represented by a Lorentzian function [44]. Thus, the simulated O *K* edge was further convolved with Lorentzian functions with the FWHM of the Γ_i and Γ_f , consecutively, to implement the natural energy broadening. The resulting O *K* edge is compared to the experimental O *K* edge EELS spectra obtained from BaSnO₃ films in Fig. 6. The match is good, further proving reliability of this analysis. The remaining discrepancies can be attributed to the fact that the O *K* edge sits on the tail of the Sn *M*_{4,5} edge and defects present in the actual samples are not accounted for in the calculations. No significant difference was observed between BaSnO₃ films on SrTiO₃ and LaAlO₃ substrates. The peak positions from experimental O *K* edge EELS spectra are in good agreement with the simulation result (Table III). This comparison allows accurate determination of the onset of the EELS O *K* edge, which represents the minimum of the conduction band, E_C , at 528.9 eV.

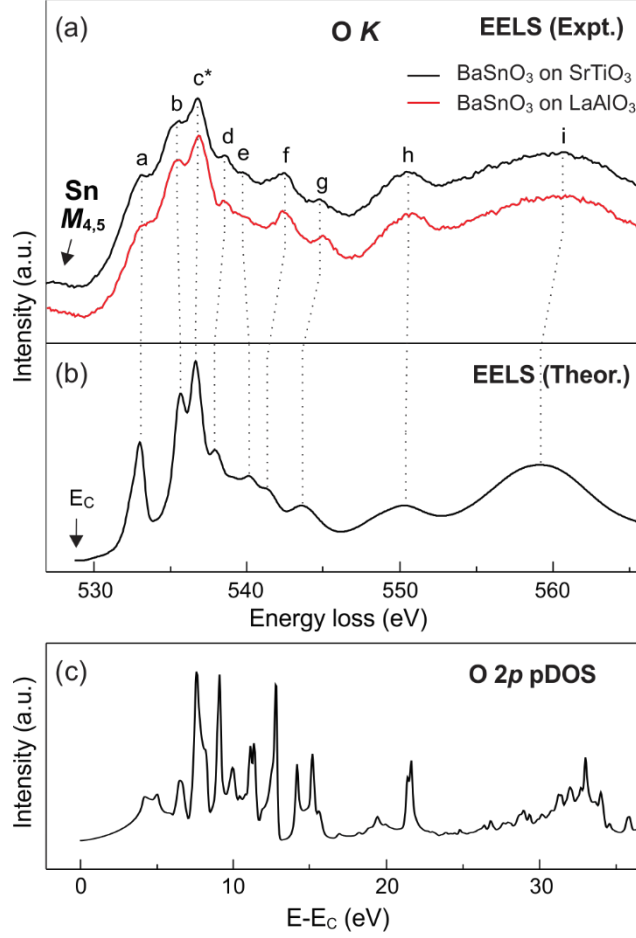


FIG. 6. Comparison of experimental EELS O K edges from BaSnO₃ films (a) and simulated O K edge (b). The peak c* was used as a reference for the alignment. The onset of the EELS O K edge representing the minimum of the conduction band, E_c , is indicated using an arrow. The identifiable peaks are labeled and compared in Table III. Note that the O K edge overlaps with the tail of the Sn $M_{4,5}$ edge. (c) The calculated O 2p pDOS of the conduction band in BaSnO₃ that was used to calculate the spectrum in (b).

TABLE III. Comparison of peak positions from the experimental and the simulated O K edge EELS shown in Fig. 6. The peak c* is used for alignment.

	Expt. (eV)	Theor. (eV)
a	533.3	533.2
b	535.5	535.8
c*	536.8	536.8
d	538.6	538.2
e	539.9	540.4
f	542.5	541.5
g	545.0	543.8
h	550.7	550.5
i	560.6	559.4

The Sn $M_{4,5}$ edge and Ba $N_{4,5}$ and $M_{4,5}$ edges were also measured. The results are shown in Fig. 7. The Ba $N_{4,5}$ edge has a delayed maximum with detectable fine structure generated by the excitation of Ba $4d$ electrons (Fig. 7(a)). The Sn $M_{4,5}$ edge, which is attributed to the excitation of Sn $3d$ electrons, is mostly positioned just before the O K edge, as shown in Fig. 7(b). The overall peak shape follows a delayed maximum shape and is similar to that from SnO₂ [57], indicating the presence of Sn in the 4+ oxidation state. Due to a high density of unfilled Ba $4f$ orbitals above the Fermi energy, the Ba $M_{4,5}$ edge appears as two strong white lines: M_5 (labeled as n) and M_4 (labeled as o), separated by 15 eV. In a simple single-electron excitation description, the two peaks are explained via spin-orbit splitting [58]. The $3d^{5/2}$ (M_5) and $3d^{3/2}$ (M_4) initial states are split due to the spin-orbit interaction, with a 6:4 ratio of degeneracy of the states [24,51]. However, the ratio of integral intensity of M_5 and M_4 in experimental EELS was observed to be 0.81 for the BaSnO₃ film on LaAlO₃ and 0.83 for the BaSnO₃ film on SrTiO₃. These values deviate considerably from the 1.5 of the 6:4 ratio of degeneracy. Also, an additional pre-peak (labeled as m) is observed ahead of the M_5 peak. This discrepancy is primarily due to the electron-hole interaction in the final state, which is not considered in the simple single-electron excitation interpretation. The atomic multiplet theory effectively incorporates such a multi-electron excitation effect, where the electron-electron interaction, H_{ee} , and the spin-orbit interaction, H_{so} , are added into the Hamiltonian of the single-electron atomic model, H_{1s} , i.e. $H = H_{1s} + H_{ee} + H_{so}$ [51,58]. When the H_{so} is negligible compared to the H_{ee} , the electronic states of an atom can be described using the LS coupling scheme, in which electronic states are determined by a given atomic configuration. By employing the LS coupling scheme, we can derive the initial and final electronic states and the available electronic transitions. Three available transitions for the excitations of Ba $4d$ electrons to Ba $4f$ orbitals can be predicted, which effectively describe the observations of the peaks, m, n, and o in the Ba $M_{4,5}$ edge as well as the low value of the M_5/M_4 ratio [58].

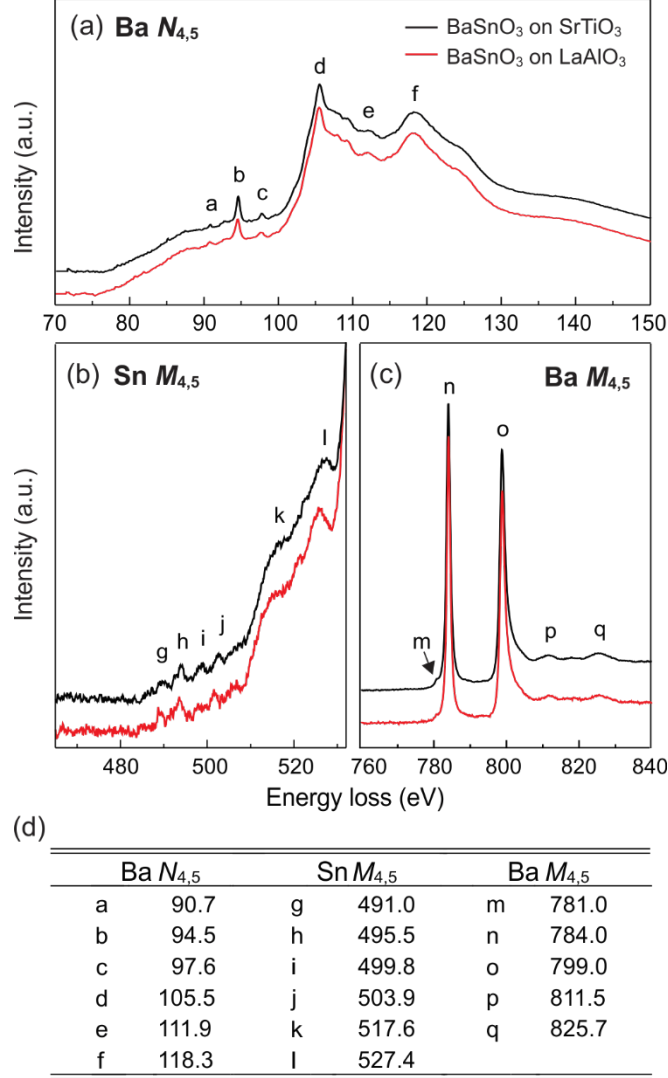


FIG. 7. Measured core-loss EELS spectra from BaSnO₃ films: (a) Ba $N_{4,5}$ edge, (b) Sn $M_{4,5}$ edge, and (c) Ba $M_{4,5}$ edge. (d) List of experimental peak positions of Ba $N_{4,5}$, Ba $M_{4,5}$, and Sn $M_{4,5}$ EELS edges fine structure shown in panels (a-c).

IV. CONCLUSION

The electronic structure of epitaxial BaSnO₃ films grown on SrTiO₃(001) and LaAlO₃(001) substrates were investigated using experimental high-energy-resolution EELS in STEM, and *ab initio* calculations. The indirect band gap energy was measured from the low-loss EELS to be 3.0 ± 0.1 eV for

the MBE-grown BaSnO₃ film on SrTiO₃ and 3.1 ± 0.2 eV for the high pressure oxygen sputtered BaSnO₃ film on LaAlO₃. Experimental low-loss EELS spectra were compared with the calculated $Im[-1/\epsilon]$ function, which is directly proportional to the electron energy-loss function, and the observed peaks due to plasmon excitations and interband transitions were analyzed. The experimental bulk plasmon peak was observed at 26.1 eV while the theoretical value was predicted to be at 26.6 eV. The expected small discrepancy between the experimental and calculated bulk plasmon energy was explained through plasmon damping, which was not properly taken into account in “phonon-free” and “defect-free” *ab initio* calculations. The interband electronic transition peaks were clearly observed and their positions were identified in low-loss EELS. The results were compared with predictions based on the calculated pDOS, where the observed peaks were assigned to distinct interband transitions from the valence band to conduction band.

The core-level electron excitations were also examined using the core-loss EELS edges. O *K*, Ba *N*_{4,5}, Sn *M*_{4,5}, and Ba *M*_{4,5} edges were measured using high-energy-resolution EELS and their fine structures were analyzed. For comparison, a simpler O *K* edge, resulting from the excitation of O 1*s* electrons to the empty DOS above the Fermi energy, was simulated from calculated O 2*p* pDOS. When the instrumental and the natural energy broadenings were implemented into this simulation, the resulting theoretical O *K* edge was in very good agreement with the experimental O *K* edges, further conforming reliability of this analysis. The number of peaks and their relative intensities in Ba *M*_{4,5} edge fine structure, which deviate from a simple spin-orbit interaction model with a 6:4 ratio of degeneracy, were explained by more rigorous atomic multiplet theory. Importantly, this work can be used as a starting point to explore the local electronic structure changes in BaSnO₃ films by structural defects, including dislocations, vacancies, interfaces, and impurity doping.

ACKNOWLEDGMENTS:

This work was supported in part by the NSF MRSEC under award number DMR-1420013, also in part by NSF DMR-1410888, NSF EAR-134866 and EAR-1319361, by Grant-in-Aid program of the University of Minnesota, and by the Defense Threat Reduction Agency, Basic Research Award #HDTRA1-14-1-0042 to the University of Minnesota. Computational resources were partly provided by Blue Waters sustained-petascale computing project, which is supported by the NSF under awards OCI-0725070 and ACI-1238993 and the state of Illinois. STEM analysis was performed in the Characterization Facility of the University of Minnesota, which receives partial support from the NSF through the MRSEC. H.Y. acknowledges a fellowship from the Samsung Scholarship Foundation, Republic of Korea.

REFERENCES:

- [1] X. Luo, Y. S. Oh, A. Sirenko, P. Gao, T. A. Tyson, K. Char, and S. W. Cheong, High carrier mobility in transparent $\text{Ba}_{1-x}\text{La}_x\text{SnO}_3$ crystals with a wide band gap, *Appl. Phys. Lett.* **100**, 172112 (2012).
- [2] H. J. Kim, U. Kim, H. M. Kim, T. H. Kim, H. S. Mun, B. Jeon, K. T. Hong, W. Lee, C. Ju, K. H. Kim, and K. Char, High mobility in a stable transparent perovskite oxide, *Appl. Phys. Express* **5**, 061102 (2012).
- [3] S. Raghavan, T. Schumann, H. Kim, J. Y. Zhang, T. A. Cain, and S. Stemmer, High-mobility BaSnO_3 grown by oxide molecular beam epitaxy, *APL Mater.* **4**, 016106 (2016).
- [4] H. M. Kim, U. Kim, C. Park, H. Kwon, and K. Char, Thermally stable pn-junctions based on a single transparent perovskite semiconductor BaSnO_3 , *APL Mater.* **4**, 056105 (2016).
- [5] U. Kim C. Park, T. Ha, Y. M. Kim, N. Kim, C. Ju, J. Park, J. Yu, J. H. Kim, and K. Char, All-perovskite transparent high mobility field effect using epitaxial BaSnO_3 and LaInO_3 , *APL Mater.* **3**, 036101 (2015).
- [6] S. Ismail-Beigi, F. J. Walker, S. W. Cheong, K. M. Rabe, and C. H. Ahn, Alkaline earth stannates: The next silicon?, *APL Mater.* **3**, 062510 (2015).
- [7] L. Zhu, Z. Shao, J. Ye, X. Zhang, X. Pan, and S. Dai, Mesoporous BaSnO_3 layer based perovskite solar cells, *Chem. Comm.* **52**, 970 (2016).

- [8] S. A. Chambers, T. C. Kaspar, A. Prakash, G. Haugstad, and B. Jalan, Band alignment at epitaxial $\text{BaSnO}_3/\text{SrTiO}_3(001)$ and $\text{BaSnO}_3/\text{LaAlO}_3(001)$ heterojunctions, *Appl. Phys. Lett.* **108**, 152104 (2016).
- [9] A. Prakash, J. Dewey, H. Yun, J. S. Jeong, K. A. Mkhoyan, and B. Jalan, Hybrid molecular beam epitaxy for the growth of stoichiometric BaSnO_3 , *J. Vac. Sci. Technol. A* **33**, 060608 (2015).
- [10] Z. Lebens-Higgins, D. O. Scanlon, H. Paik, S. Sallis, Y. Nie, M. Uchida, N. F. Quackenbush, M. J. Wahila, G. E. Sterbinsky, D. A. Arena, J. C. Woicik, D. G. Schlom, and L. F. J. Piper, Direct observation of electrostatically driven band gap renormalization in a degenerate perovskite transparent conducting oxide, *Phys. Rev. Lett.* **116**, 027602 (2016).
- [11] U. S. Alaan, P. Shafer, A. T. Diaye, E. Arenholz, and Y. Suzuki, Gd-doped BaSnO_3 : A transparent conducting oxide with localized magnetic moments, *Appl. Phys. Lett.* **108**, 042106 (2016).
- [12] J. Shiogai, K. Nishihara, K. Sato, and A. Tsukazaki, Improvement of electron mobility in $\text{La}:\text{BaSnO}_3$ thin films by insertion of an atomically flat insulating $(\text{Sr},\text{Ba})\text{SnO}_3$ buffer layer, *AIP Advances* **6**, 065305 (2016).
- [13] S. Yu, D. Yoon, and J. Son, Enhancing electron mobility in La-doped BaSnO_3 thin films by thermal strain to annihilate extended defects, *Appl. Phys. Lett.* **108**, 262101 (2016).
- [14] H. Mizoguchi, H. W. Eng, and P. M. Woodward, Probing the electronic structures of ternary perovskite and pyrochlore oxides containing Sn^{4+} or Sb^{5+} , *Inorg. Chem.* **43**, 1667 (2004).
- [15] E. Moreira, J. M. Henriques, D. L. Azevedo, E. W. S. Caetano, V. N. Freire, U. L. Fulco, and E. L. Albuquerque, Structural and optoelectronic properties, and infrared spectrum of cubic BaSnO_3 from first principles calculations, *J. Appl. Phys.* **112**, 043703 (2012).
- [16] A. Slassi, Ab initio study of a cubic perovskite: Structural, electronic, optical, and electrical properties of native, lanthanum- and antimony-doped barium tin oxide, *Mater. Sci. Semicond. Process.* **32**, 100 (2015).
- [17] S. Soleimanpour and F. Kanjouri, First principle study of electronic and optical properties of the cubic perovskite BaSnO_3 , *Physica B: Condens. Matter.* **432**, 16 (2014).
- [18] S. James Allen, S. Raghavan, T. Schumann, K. M. Law, and S. Stemmer, Conduction band edge effective mass of La-doped BaSnO_3 , *Appl. Phys. Lett.* **108**, 252107 (2016).
- [19] D. J. Singh, Q. Xu, and K. P. Ong, Strain effects on the band gap and optical properties of perovskite SrSnO_3 and BaSnO_3 , *Appl. Phys. Lett.* **104**, 011910 (2014).
- [20] T. Schumann, S. Raghavan, K. Ahadi, H. Kim, and S. Stemmer, Structure and optical band gaps of $(\text{Ba},\text{Sr})\text{SnO}_3$ films grown by molecular beam epitaxy, *J. Vac. Sci. Technol. A* **34**, 050601 (2016).

- [21] S. Prabhakar, J. B. Benjamin, C. P. Sebastian, S. Prakash, S. Sindhu, K. Devendra, and P. Om, Electronic structure, electrical and dielectric properties of BaSnO₃ below 300 K, *Jpn. J. Appl. Phys.* **47**, 3540 (2008).
- [22] K. Ganguly, P. Ambwani, P. Xu, J. S. Jeong, K. A. Mkhoyan, C. Leighton, and B. Jalan, Structure and transport in high pressure oxygen sputter-deposited BaSnO_{3- δ} , *APL Mater.* **3**, 062509 (2015).
- [23] There is some uncertainty in these thickness values measured using a typical log-ratio method because of unknown λ_p for BaSnO₃ and the presence of multiple strong peaks from interband electronic transitions, which are not accounted in the method.
- [24] R. F. Egerton, *Electron Energy Loss Spectroscopy in the Electron Microscope* (Plenum Press, New York, 1996).
- [25] P. Blaha, K. Schwarz, G. Madsen, D. Kvasnicka, J. Luitz, User's Guide, WIEN2k_14.2: An augmented plane wave plus local orbitals program for calculating crystal properties, Vienna University of Technology, 2014.
- [26] K. Schwarz, P. Blaha, and G. K. H. Madsen, Electronic structure calculations of solids using the WIEN2k package for material sciences, *Comput. Phys. Commun.* **147**, 71 (2002).
- [27] K. Schwarz and P. Blaha, Solid state calculations using WIEN2k, *Comput. Mater. Sci.* **28**, 259 (2003).
- [28] J. P. Perdew, K. Burke, and M. Ernzerhof, Generalized gradient approximation made simple, *Phys. Rev. Lett.* **77**, 3865 (1996).
- [29] P. E. Blöchl, O. Jepsen, and O. K. Andersen, Improved tetrahedron method for Brillouin-zone integrations, *Phys. Rev. B* **49**, 16223 (1994).
- [30] C. Ambrosch-Draxl and J. O. Sofo, Linear optical properties of solids within the full-potential linearized augmented planewave method, *Comput. Phys. Commun.* **175**, 1 (2006).
- [31] D. Mitchell, "HRTEM Filter," Dave Mitchell's Digital Micrograph™ Scripting Website, accessed November 5, 2016, <http://www.dmscripting.com/>.
- [32] R. Kilaas, Optimal and near-optimal filters in high-resolution electron microscopy, *J. Microsc.* **190**, 45 (1998).
- [33] H. Raether, *Excitation of plasmons and interband transitions by electrons*, (Springer-Verlag, Berlin, 1980).
- [34] C. Kittel, *Introduction to Solid State Physics* (Wiley, New Jersey, 1996).

- [35] G. Brockt and H. Lakner, Nanoscale EELS analysis of dielectric function and bandgap properties in GaN and related materials, *Micron* **31**, 435 (2000).
- [36] P. Moreau and M. C. Cheynet, Improved comparison of low energy loss spectra with band structure calculations: the example of BN filaments, *Ultramicroscopy* **94**, 293 (2003).
- [37] V. J. Keast, Ab initio calculations of plasmons and interband transitions in the low-loss electron energy-loss spectrum, *J. Electron. Spectrosc. Relat. Phenom.* **143**, 97 (2005).
- [38] Y. Sato, M. Terauchi, M. Mukai, T. Kaneyama, and K. Adachi, High energy-resolution electron energy-loss spectroscopy study of the dielectric properties of bulk and nanoparticle LaB₆ in the near-infrared region, *Ultramicroscopy* **111**, 1381 (2011).
- [39] B. G. Kim, J. Y. Jo, and S. W. Cheong, Hybrid functional calculation of electronic and phonon structure of BaSnO₃, *J. Solid State Chem.* **197**, 134 (2013).
- [40] Y. Li, L. Zhang, Y. Ma, and D. J. Singh, Tuning optical properties of transparent conducting barium stannate by dimensional reduction, *APL Mater.* **3**, 011102 (2015).
- [41] K. van Benthem, C. Elsässer, and R. H. French, Bulk electronic structure of SrTiO₃: Experiment and theory, *J. Appl. Phys.* **90**, 6156 (2001).
- [42] B. Hadjarab, A. Bouguelia, and M. Trari, Optical and transport properties of lanthanum-doped stannate BaSnO₃, *J. Phys. D: Appl. Phys.* **40**, 5833 (2007).
- [43] H. J. Kim, U. Kim, T. H. Kim, J. Kim, H. M. Kim, B. Jeon, W. Lee, H. S. Mun, K. T. Hong, J. Yu, K. Char, and K. H. Kim, Physical properties of transparent perovskite oxides (Ba,La)SnO₃ with high electrical mobility at room temperature, *Phys. Rev. B* **86**, 165205 (2012).
- [44] G. K. Wertheim, M. A. Butler, K. W. West, and D. N. E. Buchanan, Determination of the Gaussian and Lorentzian content of experimental line shapes, *Rev. Sci. Instrum.* **45**, 1369 (1974).
- [45] J. Park, S. Heo, J.G. Chung, H. Kim, H. Lee, K. Kim, and G.S. Park, Bandgap measurement of thin dielectric films using monochromated STEM-EELS, *Ultramicroscopy* **109**, 1183 (2009).
- [46] L. Gu, V. Srot, W. Sigle, C. Koch, P. Aken, F. Scholz, S. B. Thapa, C. Kirchner, M. Jetter, and M. Rühle, Band-gap measurements of direct and indirect semiconductors using monochromated electrons, *Phys. Rev. B* **75**, 195214 (2007).
- [47] F. Vaz, N. Martin, and M. Fenker, *Metallic oxynitride thin films by reactive sputtering and related deposition methods: Processes, properties and applications*, (Bentham Science Publishers, Sharjah, 2013).

- [48] A. Woessner, M. B. Lundeberg, Y. Gao, A. Principi, P. Alonso-Gonzalez, M. Carreaga, K. Watanabe, T. Taniguchi, G. Vignale, M. Polini, J. Hone, R. Hillenbrand, and F. H. L. Koppens, Highly confined low-loss plasmons in graphene–boron nitride heterostructures, *Nat. Mater.* **14**, 421 (2015).
- [49] If accuracy is not critical, the bulk plasmon energy can also be estimated using a simple free electron model with the equation, $E_p = \hbar\sqrt{ne^2/m_e\epsilon_0}$, where n is the bulk density of valence electrons, e is the charge of an electron, m_e is the mass of an electron, and ϵ_0 is the vacuum permittivity. From this free electron model, the bulk plasmon energy of valence electrons in BaSnO₃ was calculated to be 26.0 eV, which is in reasonably good agreement with the experimental bulk plasmon energy. The n used for this calculation was $4.90\times 10^{29} \text{ m}^{-3}$.
- [50] C. C. Ahn and O. L. Krivanek, *EELS atlas: A reference collection of electron energy loss spectra covering all stable elements* (Gatan, Warrendale, 1983).
- [51] F. de Groot and A. Kotani, *Core level spectroscopy of solids* (CRC Press, Boca Raton, 2008).
- [52] D. A. Muller, D. J. Singh, and J. Silcox, Connections between the electron energy-loss spectra, the local electronic structure, and the physical properties of a material: A study of nickel aluminum alloys, *Phys. Rev. B* **57**, 8181 (1998)
- [53] K. A. Mkhoyan, J. Silcox, E. S. Alldredge, N. W. Ashcroft, H. Lu, W. J. Schaff, and L. F. Eastman, Measuring electronic structure of wurtzite InN using electron energy loss spectroscopy, *Appl. Phys. Lett.* **82**, 1407 (2003)
- [54] K. Jorissen, Ph. D. thesis, Univ. of Antwerp, 2007.
- [55] R. F. Egerton, New techniques in electron energy-loss spectroscopy and energy-filtered imaging, *Micron* **34**, 127 (2003).
- [56] M. O. Krause, Atomic radiative and radiationless yields for K and L shells, *J. Phys. Chem. Ref. Data* **8**, 307 (1979).
- [57] M. S. Moreno, R. F. Egerton, and P. A. Midgley, Differentiation of tin oxides using electron energy-loss spectroscopy, *Phys. Rev. B* **69**, 233304 (2004).
- [58] S. J. Pennycook and P. D. Nellist, *Scanning transmission electron microscopy: Imaging and analysis* (Springer, New York, 2011).